

## Article

# Vibration Energy Harvesting from Plates by Means of Piezoelectric Dynamic Vibration Absorbers

Michele Tonan , Alberto Pasetto  and Alberto Doria \* 

Department of Industrial Engineering, University of Padova, 35131 Padova, Italy;  
michele.tonan@phd.unipd.it (M.T.); alberto.pasetto.2@phd.unipd.it (A.P.)

\* Correspondence: alberto.doria@unipd.it; Tel.: +39-049-827-6803

**Abstract:** In this paper, the possibility of harvesting energy from the vibrations of a plate is analyzed. The harvester takes the form of a cantilever dynamic vibration absorber equipped with a piezoelectric layer and tuned by means of a tip mass to the first mode of vibration of the plate. A mathematical model of the coupled system composed of the plate and the harvester is presented. The validity of the proposed harvester is proved by means of simulations carried out with the modal expansions approach. Simulation results highlighting the effects of harvester tuning and location are presented as well. Then, the validity of the harvester is confirmed by experimental tests carried out both with a concentrated impulsive load and with a distributed pressure load. Simulations and experimental tests are performed on the cantilever piezoelectric dynamic vibration absorber and on the same piezoelectric layer directly bonded to the plate surface. Results show an improvement in terms of generated voltage when the proposed novel device is used in place of the simple layer.

**Keywords:** piezoelectric harvester; plate vibrations; dynamic vibration absorber



**Citation:** Tonan, M.; Pasetto, A.; Doria, A. Vibration Energy Harvesting from Plates by Means of Piezoelectric Dynamic Vibration Absorbers. *Appl. Sci.* **2024**, *14*, 402. <https://doi.org/10.3390/app14010402>

Academic Editor: Alessandro Ruggiero

Received: 14 December 2023

Revised: 26 December 2023

Accepted: 30 December 2023

Published: 1 January 2024



**Copyright:** © 2024 by the authors. Licensee MDPI, Basel, Switzerland. This article is an open access article distributed under the terms and conditions of the Creative Commons Attribution (CC BY) license (<https://creativecommons.org/licenses/by/4.0/>).

## 1. Introduction

The present era, which is characterized by IoT and Industry 4.0, requires a lot of sensors to monitor industrial, urban and natural environments. The use of wiring to feed the sensors is sometimes unfeasible, e.g., this is the case of remote sensors installed in buoys in deep sea or in tall buildings and antennas. Nowadays, remote sensors nodes are fed by means of batteries, which are not eco-friendly and require complex and expensive replacement operations. Fortunately, the energy consumption of sensor nodes is constantly decreasing, and new technical solutions are possible. Vibration energy harvesting is a great opportunity since remote sensors can be fed by using existing sources of energy. Vibration energy harvesting can be performed by exploiting different physical phenomena to convert mechanical energy into electrical energy. In the scientific literature, piezoelectric [1], electromagnetic [2], electrostatic [3] and triboelectric [4,5] harvesters have been proposed. Piezoelectric harvesters usually take the form of thin layers that are either bonded to a vibrating surface or are bonded to a cantilever beam to make a cantilever harvester. Piezoelectric harvesters generate high voltage, can be integrated with the vibrating structure and have small mass and encumbrance. For these reasons, they are adopted to feed sensors and other small electronic equipment in vehicles, industrial machinery, civil structures and biomedical devices.

The vibrating plate is one of the most common vibrating structures and is a typical part of machines, domestic appliances, road vehicles, trains and aircraft [6,7]. Vibrating plates can be found in buildings (panels of facades) and in other civil structures as well [8,9]. Hence, harvesting vibration energy from plates is a very present research topic. Plates are sometimes excited by concentrated loads, but there are many cases in which this structure is excited by the distributed loads caused by wind, traffic or water flows. The simplest piezoelectric harvester for a vibrating plate is a piezoelectric layer directly bonded to the

plate surface. It works in the bending mode (the 3-1 mode [10]) and exploits the strain caused by plate bending. The strain of the plate reaches the maximum value at the natural frequencies of the modes of vibrations that are excited by concentrated or distributed loads. A cantilever harvester with its tip mass tuned to the natural frequency of the most excited mode of vibration of the plate is a possible alternative that enables better exploitation of the resonance phenomenon. This cantilever harvester behaves as a dynamic vibration absorber (DVA) that is able to receive a large amount of energy from the plate. On the one hand, plate vibrations are strongly reduced [11]; on the other hand, the cantilever harvester experiences large-amplitude vibrations.

It is worth noting that the principle of DVAs has been also adopted by several researchers to develop devices able to improve or extend the performance of simple harvesters. These devices include dynamic magnifiers [12–14], trimming oscillators [15] and inertial amplifiers [16,17].

DVAs with piezoelectric layers have been studied in recent years both with the aim of suppressing the vibrations of the host structure and with the aim of scavenging energy. Ali and Adhikari in 2013 [18] proposed an energy harvesting DVA and analytically studied the coupling of this device with a one-degree-of-freedom (DOF) vibrating system. A lumped parameter 1-DOF model of the piezoelectric harvester was adopted. An analytical expression of the natural frequencies of the coupled system was given, the presence of two resonance peaks was demonstrated, and the influence of the piezoelectric layer on the damping of the DVA was highlighted. Abdelmoula et al. in 2017 [19] studied the coupling of a cantilever harvester with a 1-DOF vibrating system. The cantilever harvester was modeled according to the modal expansion approach like in [20]. A strategy was proposed to minimize the vibrations of the host structure and to maximize the harvested power. Experimental results dealing with the effect of a cantilever piezoelectric dynamic absorber mounted on a vibrating rigid beam were presented by Sulaiman et al. in 2021 [21]. Rezaei et al. in 2022 [22] extended the previous analyses by considering the coupling between a flexible beam and a cantilever harvester. Both the cantilever harvester and the flexible beam were modeled by adopting the modal expansion approach. The number of modes of vibration of the host structure and of the cantilever harvester that were needed to accurately model the system's dynamics was investigated. Results showed that considering only the first mode of the host structure and of the cantilever harvester is enough to capture the main features of the system. In 2012, Rajarathinam and Ali [23] improved the analysis of a 2-DOF system composed of a host vibrating structure and an energy harvesting DVA by considering both random excitation and system uncertainties. Results showed that uncertainties in the natural frequency lead to a decrease in the harvested power. Recently, Rezaei et al. [24] presented experimental results dealing with a flexible beam equipped with a cantilever harvester and excited by a shaker. They developed a detailed integrated mode taking into account shaker dynamics. Good agreement between experimental and analytical results was obtained.

The effect of a piezoelectric DVA on a vibrating plate was not addressed in the above-mentioned research. Hence, the first aim of this paper is to study vibration energy harvesting from a vibrating plate by means of a cantilever piezoelectric dynamic vibration absorber (CPDVA). The second aim of this paper is to study the performance of a CPDVA installed on a plate excited by distributed loads that are very common in actual structures. The third aim of this paper is to make a comparison between the performances of a simple piezoelectric layer and a CPDVA mounted on the same plate.

The paper is organized as follows. In Section 2, the mathematical model of a vibrating plate with a CPDVA is developed: plate dynamics are modeled with the modal expansion approach, whereas the harvester is modeled with a lumped parameter approach that takes into account the first mode of vibration. In Section 3, some calculated results are presented that show the effect of harvester tuning and positioning on the generated voltage. The experimental setup is described in Section 4. A prototype CPDVA was built using a commercial cantilever harvester M2814P2C-01 made by Smart Material GmbH. This device

was installed in a clamped–clamped–free–free plate excited by concentrated and distributed loads. Section 5 deals with experimental results and focuses on the comparison between the voltage generated by the CPDVA and the one generated by a simple piezoelectric layer directly bonded to the plate. Finally, conclusions are drawn in Section 6.

## 2. Mathematical Model

In this study, a flat rectangular aluminum plate with two opposite free sides and that is clamped on the other two sides is considered. The system and the main dimensions are represented in Figure 1. The plate lies on the  $x$ - $y$  plane, and vibrations occur in the  $z$  direction. The cantilever piezoelectric dynamic vibration absorber (CPDVA) is composed of a cantilever beam with its axis parallel to the plate and fixed to the plate through one of its extremities. A tip mass is attached to the free end of the cantilever for tuning. Concentrated and distributed loads in the  $z$  direction are considered since they excite the vibrations of the plate in the transversal direction. The vibrations are then transferred to the CPDVA, which harvests energy through the piezoelectric patch attached to the cantilever.

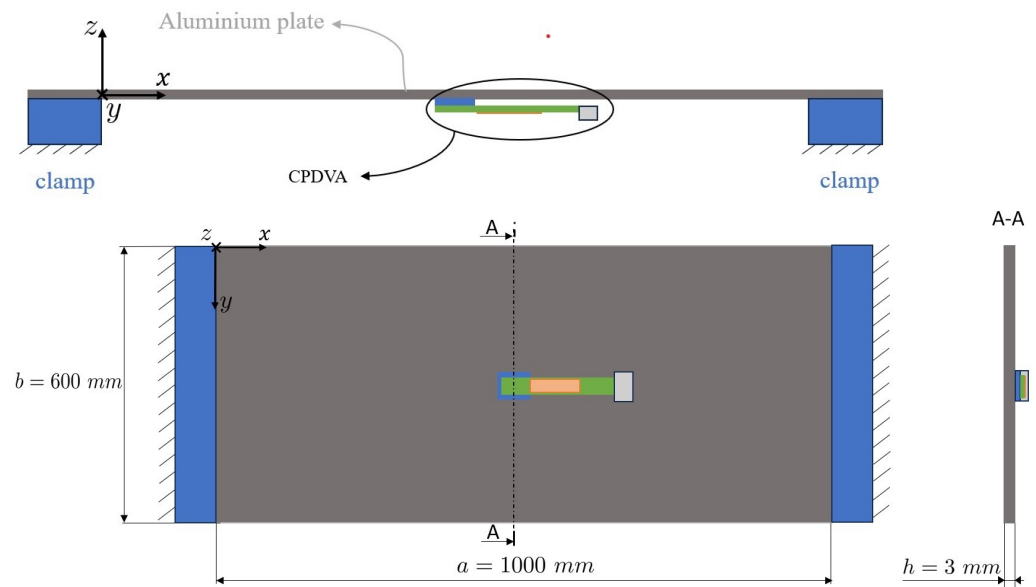


**Figure 1.** Energy harvesting system (top). Bottom and section views of the plate equipped with the CPDVA (bottom).

### 2.1. Plate Model

The equation of the forced vibrations of a plate is:

$$\rho \ddot{w}(x, y, t) + C_{plate} \dot{w}(x, y, t) + D \left( \frac{\partial^4 w(x, y, t)}{\partial x^4} + 2 \frac{\partial^4 w(x, y, t)}{\partial x^2 \partial y^2} + \frac{\partial^4 w(x, y, t)}{\partial y^4} \right) = F(x, y, t) \quad (1)$$

where  $w$  is the transversal displacement of any point of the plate, which is a function of time and space,  $F(x, y, t)$  is a force distribution,  $\rho$  is the surface density of the plate,  $D$  is the flexural rigidity of the plate, and  $C_{plate}$  is a damping coefficient; proportional damping is assumed. The plate has homogeneous thickness  $h$ , and the flexural rigidity can be calculated from the modulus of elasticity  $E$  and from Poisson's ratio  $\nu$  as  $D = Eh^3 / (12(1 - \nu^2))$ .

Vibration modes of the plate can be found through the associated homogeneous Equation (1). According to the Rayleigh method, when the  $i$ -th mode of the plate is considered, which has  $m$  nodal lines in the  $x$  direction and  $n$  nodal lines in the  $y$  direction, the transversal displacement of each point of the rectangular plate can be expressed by the function:

$$\Phi_i(x, y) \equiv \Phi_{mn}(x, y) = X_m(x)Y_n(y) \quad (2)$$

where  $X_m(x)$  and  $Y_n(y)$  are the fundamental mode shapes along the  $x$  and  $y$  directions, respectively, and depend on the boundary conditions of the plate. For a rectangular plate clamped at  $x = 0$  and  $x = a$  and free at  $y = 0$  and  $y = b$ , the  $X_m(x)$  functions are:

$$X_m(x) = \begin{cases} \cos\left(\gamma_1 \cdot \left(\frac{x}{a} - \frac{1}{2}\right)\right) + \frac{\sin(\gamma_1/2)}{\sinh(\gamma_1/2)} \cosh\left(\gamma_1 \cdot \left(\frac{x}{a} - \frac{1}{2}\right)\right), & m = 2, 4, 6, \dots \\ \sin\left(\gamma_2 \cdot \left(\frac{x}{a} - \frac{1}{2}\right)\right) - \frac{\sin(\gamma_2/2)}{\sinh(\gamma_2/2)} \sinh\left(\gamma_2 \cdot \left(\frac{x}{a} - \frac{1}{2}\right)\right), & m = 3, 5, 7, \dots \end{cases} \quad (3)$$

where  $\gamma_1$  and  $\gamma_2$  are, respectively, the roots of:

$$\tan\left(\frac{\gamma_1}{2}\right) + \tanh\left(\frac{\gamma_1}{2}\right) = 0 \quad (4)$$

$$\tan\left(\frac{\gamma_2}{2}\right) - \tanh\left(\frac{\gamma_2}{2}\right) = 0 \quad (5)$$

The functions  $Y_n(y)$  are defined as:

$$Y_n(y) = \begin{cases} 1, & n = 0 \\ 1 - \frac{2y}{b}, & n = 1 \\ \cos\left(\gamma_1 \cdot \left(\frac{y}{b} - \frac{1}{2}\right)\right) - \frac{\sin(\gamma_1/2)}{\sinh(\gamma_1/2)} \cosh\left(\gamma_1 \cdot \left(\frac{y}{b} - \frac{1}{2}\right)\right), & n = 2, 4, 6, \dots \\ \sin\left(\gamma_2 \cdot \left(\frac{y}{b} - \frac{1}{2}\right)\right) + \frac{\sin(\gamma_2/2)}{\sinh(\gamma_2/2)} \sinh\left(\gamma_2 \cdot \left(\frac{y}{b} - \frac{1}{2}\right)\right), & n = 3, 5, 7, \dots \end{cases} \quad (6)$$

The following orthogonality conditions hold for plate modes:

$$\int_0^a \int_0^b \rho \Phi_j(x, y) \Phi_i(x, y) dx dy = m_i \delta_{ij} \quad (7)$$

$$\int_0^a \int_0^b \Phi_j(x, y) \nabla^4 \Phi_i(x, y) dx dy = \omega_i^2 \delta_{ij} \quad (8)$$

where  $\delta_{ij}$  is equal to 1 if  $i = j$  and 0 otherwise;  $m_i$  and  $\omega_i$  are the modal mass and the natural angular frequency of the mode  $i$ , respectively; and the operator  $\nabla^4$  is defined as  $\nabla^4 = \frac{\partial^4}{\partial x^4} + 2 \frac{\partial^4}{\partial x^2 \partial y^2} + \frac{\partial^4}{\partial y^4}$ .

The parameters of the plate considered in this study are summarized in Table 1. It is worth noting that the properties of the material influence the natural frequencies of the plate. However, the mathematical model is still valid with different materials of the plate.

**Table 1.** Parameters of the plate.

Parameter	Value
$a$	1 m
$b$	0.6 m
$h$	$3 \times 10^{-3}$ m
$E$	$6.9 \times 10^{10}$ Pa
$\nu$	0.33

From the plate parameters, the natural frequency and shape of each mode can be determined (for the calculation of natural frequencies, refer to [25]). In this paper, only the first six modes of the plate will be used to describe plate dynamics; the natural frequencies and the corresponding  $m$ - $n$  combinations are reported in Table 2, and Figure 2 shows the modal shapes.

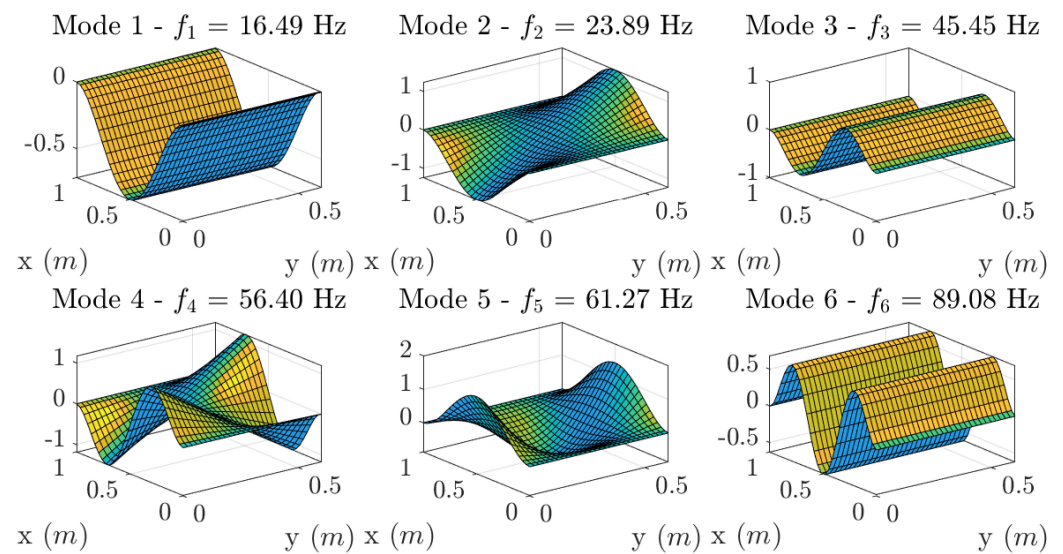


**Figure 2.** Calculated modes of vibration of the plate.

**Table 2.** Calculated natural frequency and  $m$ - $n$  combination for the first six plate modes.

Mode Number ( $i$ )	$m$	$n$	Frequency (Hz)
1	2	0	16.49
2	2	1	23.89
3	3	0	45.45
4	3	1	56.40
5	2	2	61.27
6	4	0	89.08

## 2.2. Harvester Lumped Element Model

The CPDVA is a cantilever beam partially covered by a piezoelectric layer. The cantilever is fixed to the plate at coordinates  $(x_a, y_a)$ , and a tip mass is fixed at the cantilever tip. Figure 3 represents the harvester and its geometrical parameters.

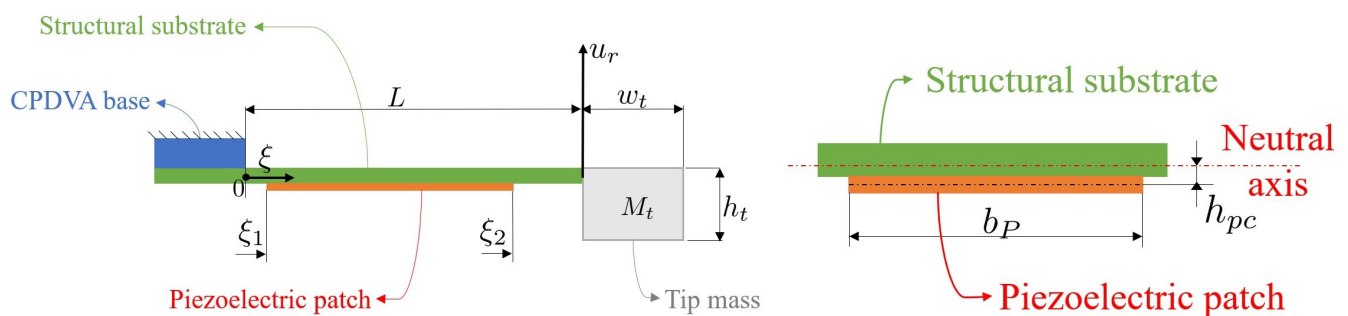


**Figure 3.** Scheme of the CPDVA (left) and harvester cross section (right).

The harvester is modeled through a single-degree-of-freedom (SDOF) approach; the variable that describes the configuration of the harvester is the tip displacement with respect to the harvester base ( $u_r(t)$ ). The equation of motion of the harvester subject to base excitation is:

$$M\ddot{u}_r(t) + C\dot{u}_r(t) + Ku_r(t) = -\alpha M\ddot{w}(x_a, y_a, t) \quad (9)$$

where  $M$ ,  $C$  and  $K$  are the lumped mass, damping and stiffness of the harvester, respectively;  $\alpha$  is a corrective factor for base excitation in SDOF models [1,10].

The lumped parameters are calculated following the approach used and validated in [26]. First of all, the displacement of the cantilever along the beam axis is expressed as the product between a shape function  $g(\xi)$  and the relative tip displacement:

$$u(\xi, t) = g(\xi)u_r(t) \quad (10)$$

where  $\xi$  is the coordinate along the beam axis:  $\xi$  is zero at the clamp location and increases moving to the tip. The static deformed shape of a cantilever with a concentrated load on its tip is assumed to approximate the shape of the first mode of the harvester. Therefore,  $g(\xi)$  is defined as:

$$g(\xi) = \frac{3\xi^2L - \xi^3}{2L^3} \quad (11)$$

where  $L$  is the length of the cantilever. Moreover, with this assumption, the ratio between tip rotation ( $\varphi$ ) and tip displacement is:

$$\frac{\varphi}{u_r} = \frac{3}{2L} \quad (12)$$

Using the Lagrangian approach, the following expressions for the lumped parameters of the harvester are found:

$$M = \frac{33}{140}(m_s + m_p) + M_t \left(1 + \frac{3w_t}{4L}\right)^2 + \frac{M_t}{8L}(h_t^2 + w_t^2) \quad (13)$$

$$K = \frac{3E_h I_h}{L^3} + \frac{\theta^2}{C_p} \quad (14)$$

$$C = 2\zeta\sqrt{KM} \quad (15)$$

where  $m_s$  and  $m_p$  are the masses of the structural and piezoelectric layers of the cantilever, respectively;  $M_t$ ,  $w_t$  and  $h_t$  are the mass, width and height of the tip mass;  $E_h I_h$  is the equivalent bending stiffness of the beam;  $C_p$  is the capacitance of the piezoelectric layer;  $\theta$  is the electro-mechanical coupling coefficient; and  $\zeta$  is the damping coefficient of the harvester. It is worth noting that stiffness  $K$  depends on the backward piezoelectric effect as well.

In open circuit conditions, the electro-mechanical coupling coefficient is defined by the following equation ([20]):

$$\theta = -e_{3,1}b_ph_{pc} \int_{\xi_1}^{\xi_2} \frac{d^2g(\xi)}{d\xi^2} d\xi \quad (16)$$

where  $e_{3,1}$  is the piezoelectric constant of the material;  $b_p$  is the width of the piezoelectric layer;  $h_{pc}$  is the distance between the neutral axis of the composite beam and the center of the piezoelectric layer; and  $\xi_1$ ,  $\xi_2$  are the coordinates that identify the extremities of the piezoelectric layer along the beam axis, see Figure 3.

Finally, the open-circuit voltage produced by the harvester is expressed as [26]:

$$v_{oc}(t) = \frac{\theta}{C_p}u_r(t) \quad (17)$$

Piezoelectric energy harvesters provide alternating voltage (AC), but most electronic devices require a DC voltage input. Hence, piezoelectric energy harvesters are equipped with specific converting systems [27]. Open-circuit voltage is considered in this paper since it is an important parameter for the design of these converting system.



### 2.3. Coupled Equations

The aim of this section is to calculate the frequency response functions (FRFs) between applied loads, generated voltage and plate displacement, since they make possible the calculation of the response of the system in the presence of harmonic, periodic, transient and random loads. To generalize the analysis, the following loads acting on the plate are considered: a uniform distributed load  $q_z(t)$ , a concentrated force  $F_c(t)$  applied at the point of coordinates  $(x_c, y_c)$  and the forcing term due to the CPDVA  $F_a(t)$ . The uniform distributed load can represent both the action of a fluid in contact with the plate and an inertial load resulting from the acceleration of the two clamped sides of the plate ( $\ddot{z}_f(t)$ ) due to environmental vibrations. In this case:

$$q_z(t) = -\rho \ddot{z}_f(t) \quad (18)$$

The concentrated force is a reference load condition that simulates the effect of impulsive tests carried out by means of hammers for modal testing.

The force due to the CPDVA is the sum of two terms. The first term is the inertial force related to the oscillation of the harvester base, which has mass  $M_a$  and is rigidly fixed to the plate. The second term is related to the oscillation of the cantilever with a tip mass. The second term can be obtained by isolating the damping and the stiffness terms in Equation (9). Therefore, the following expression is found:

$$F_a(t) = -M \left( \ddot{u}_r(t) + \left( \alpha + \frac{M_a}{M} \right) \ddot{w}(x_a, y_a, t) \right) \quad (19)$$

In order to obtain the equations of motion of the system composed of the plate and the CPDVA, the distributed and the concentrated forces are inserted in (1), and the resulting equation is combined with (9):

$$\begin{cases} \rho \ddot{w}(x, y, t) + C_{plate} \dot{w}(x, y, t) + D \nabla^4 w(x, y, t) = q_z(t) + F_c(t) \delta(x - x_c) \delta(y - y_c) + F_a(t) \delta(x - x_a) \delta(y - y_a) \\ M \ddot{u}_r(t) + C \dot{u}_r(t) + K u_r(t) = -\alpha M \ddot{w}(x_a, y_a, t) \end{cases} \quad (20)$$

where  $\delta$  is the Dirac delta function.

The transversal displacement of the plate is expressed as a linear combination of the modes of the plate. In particular, the modes of vibration of the clamped–clamped–free–free plate described in Section 2.1 are adopted:

$$w(x, y, t) = \sum_{i=1}^{\infty} \Phi_i(x, y) \eta_i(t) \quad (21)$$

where  $\eta_i(t)$  is the modal coordinate of mode  $i$ . In practical simulations, the summation in (21) is truncated by taking into account only the first  $N$  modes of the plate in the frequency band of interest. Substituting (19) and (21) in (20) gives:

$$\begin{cases} \rho \sum_{i=1}^N \Phi_i(x, y) \ddot{\eta}_i(t) + C_{plate} \sum_{i=1}^N \Phi_i(x, y) \dot{\eta}_i(t) + D \nabla^4 \sum_{i=1}^N \Phi_i(x, y) \eta_i(t) = q_z(t) + F_c(t) \delta(x - x_c) \delta(y - y_c) - \\ M \left( \ddot{u}_r(t) + \left( \alpha + \frac{M_a}{M} \right) \sum_{i=1}^N \Phi_i(x_a, y_a) \ddot{\eta}_i(t) \right) \delta(x - x_a) \delta(y - y_a) \\ M \ddot{u}_r(t) + C \dot{u}_r(t) + K u_r(t) = -\alpha M \sum_{i=1}^N \Phi_i(x_a, y_a) \ddot{\eta}_i(t) \end{cases} \quad (22)$$

Then, the orthogonality conditions (7) and (8) are exploited by multiplying (22) for the generic mode  $\Phi_i(x, y)$  and integrating on the whole plate. In this way, the following system of  $N + 1$  differential equations in modal coordinates is obtained:

$$\begin{cases} m_i \ddot{\eta}_i(t) + 2m_i \zeta_i \omega_i \dot{\eta}_i(t) + m_i \omega_i^2 \eta_i(t) = \int_0^a \int_0^b \Phi_i(x, y) q_z(t) dx dy + \Phi_i(x_c, y_c) F_c(t) - \\ M \Phi_i(x_a, y_a) \left( \ddot{u}_r(t) + \left( \alpha + \frac{M_a}{M} \right) \sum_{i=1}^N \Phi_i(x_a, y_a) \ddot{\eta}_i(t) \right) \\ M \ddot{u}_r(t) + C \dot{u}_r(t) + K u_r(t) = -\alpha M \sum_{i=1}^N \Phi_i(x_a, y_a) \ddot{\eta}_i(t) \end{cases} \quad (23)$$

where the first equation holds for  $i = 1, 2, \dots, N$ .

For the computation of the frequency response functions (FRFs), the following harmonic solutions are assumed:

$$\eta_i(t) = \eta_{i,0} \cdot e^{i\omega t} \quad (24)$$

$$u_r(t) = u_{r,0} \cdot e^{i\omega t} \quad (25)$$

$$q_z(t) = q_{z,0} \cdot e^{i\omega t} \quad (26)$$

$$F_c(t) = F_{c,0} \cdot e^{i\omega t} \quad (27)$$

where  $i$  is the imaginary unit.

Introducing (24)–(27) in (23), this system of linear equations holds:

$$\begin{cases} -\omega^2 m_i \eta_{i,0} + 2i \omega m_i \zeta_i \omega_i \eta_{i,0} + m_i \omega_i^2 \eta_{i,0}(t) = \int_0^a \int_0^b \Phi_i(x, y) q_{z,0} dx dy + \Phi_i(x_c, y_c) F_{c,0} + \\ \omega^2 M \Phi_i(x_a, y_a) \left( u_{r,0} + \left( \alpha + \frac{M_a}{M} \right) \sum_{i=1}^N \Phi_i(x_a, y_a) \eta_{i,0} \right) \\ -\omega^2 M u_{r,0} + i \omega C u_{r,0} + K u_{r,0} = \omega^2 \alpha M \sum_{i=1}^N \Phi_i(x_a, y_a) \eta_{i,0} \end{cases} \quad (28)$$

where the first equation holds for  $i = 1, 2, \dots, N$ .

System (28) is rearranged by letting the unknown  $\eta_{1,0}, \eta_{2,0}, \dots, \eta_{N,0}$  and  $u_{r,0}$  be on the left side and moving the assigned forcing terms to the right side. Moreover, for brevity, the following symbols are adopted:

$$\Phi_i^a = \Phi_i(x_a, y_a)$$

$$\Phi_i^c = \Phi_i(x_c, y_c)$$

$$A_i = -m_i \omega^2 + 2i m_i \zeta_i \omega_i \omega + m_i \omega_i^2$$

$$B_i = M \omega^2 \Phi_i^a \left( \alpha + \frac{M_a}{M} \right) \quad (29)$$

$$P_i = \int_0^a \int_0^b \Phi_i(x, y) dx dy$$

$$D = -M \omega^2 + i C \omega + K$$

Therefore:

$$\begin{cases} (A_i - \Phi_i^a B_i) \eta_{i,0} - \Phi_i^a \sum_{j=1}^n B_j \eta_{j,0} (1 - \delta_{ij}) - B_i \frac{M}{\alpha M + M_a} u_{r,0} = P_i q_{z,0} + \Phi_i^c F_{c,0} \\ -\alpha M \omega^2 \sum_{i=1}^n \Phi_i^a \eta_{i,0} + D u_{r,0} = 0 \end{cases} \quad (30)$$

where the first equation holds for  $i = 1, 2, \dots, N$ .



Considering the uniform distributed load amplitude  $q_{z,0}$  or the concentrated force amplitude  $F_{c,0}$  as inputs, Equation (30) can be solved for a range of forcing frequencies  $\omega$  and amplitudes  $\eta_{1,0}, \eta_{2,0}, \dots, \eta_{N,0}$ , and  $u_{r,0}$  can be obtained at each frequency. The amplitude of the plate displacement  $w_0$  can be calculated from the modal coordinates by means of:

$$w_0(x, y, \omega) = \sum_{i=1}^N \Phi_i(x, y) \eta_{i,0}(\omega) \quad (31)$$

Therefore, FRFs between the plate displacement (and acceleration) at the generic point  $x_P, y_P$  and the loads can be calculated using the following definitions:

$$FRF_{w_P, q_z}(\omega) = \frac{w_0(x_P, y_P, \omega)}{q_{z,0}} \quad FRF_{\ddot{w}_P, q_z}(\omega) = -\omega^2 \frac{w_0(x_P, y_P, \omega)}{q_{z,0}} \quad (32)$$

$$FRF_{w_P, F_c}(\omega) = \frac{w_0(x_P, y_P, \omega)}{F_{c,0}} \quad FRF_{\ddot{w}_P, F_c}(\omega) = -\omega^2 \frac{w_0(x_P, y_P, \omega)}{F_{c,0}} \quad (33)$$

where (32) are used for the uniform distributed load, and (33) are used for the concentrated load.

The amplitude of the open-circuit (OC) voltage can be retrieved by exploiting Equation (17); the following expression holds:

$$v_{oc,0} = \frac{\theta}{C_p} u_{r,0} \quad (34)$$

Finally, the FRFs between the OC voltage and applied loads are:

$$FRF_{v, q_z}(\omega) = \frac{v_{oc,0}(\omega)}{q_{z,0}} \quad (35)$$

$$FRF_{v, F_c}(\omega) = \frac{v_{oc,0}(\omega)}{F_{c,0}} \quad (36)$$

for cases with distributed and concentrated loads, respectively. The mathematical model was implemented in MATLAB, and in particular, the modes of vibration were integrated using the symbolic toolbox.

### 3. Calculated Results

The first mode of vibration of a plate has the largest probability of being stimulated by environmental sources of excitation (wind, traffic and rain) for two reasons: the frequency and the modal shape.

Typically, environmental sources are characterized by power spectral densities (PSDs) showing the maximum amplitudes in the low frequency range. Turbulence of grazing flows used to collect energy from artificial piezoelectric grass [28] shows relevant PSD amplitudes below 50 Hz. Wind turbulence PSDs used for the design of civil structures show maximum amplitudes below 1 Hz [29–31]. The PSDs of traffic-induced vibrations show their main peaks below 20 Hz [32].

The first mode of vibration of a clamped–clamped–free–free plate has the simplest modal shape (Figure 2). Higher-order modes show an increasing number of nodal lines that define different zones of the plate that vibrate in phase opposition. A spatially uniform pressure fluctuation on the surface of the plate can excite the first mode of vibration but is not able to transfer much energy to higher-order modes with different areas that vibrate in phase opposition. To highlight this concept, the FRF between the acceleration of the point at the center of the plate and the distributed load  $q_z(t)$  was calculated by means of the mathematical model of Section 2. The FRF magnitude, which is plotted in Figure 4, shows that only the first and sixth modes of vibration are excited by the distributed load. The other modes are not excited at all because there is a complete cancellation between the pressure loads applied in the areas of the plate that move in opposition. Owing to the dependence

on the frequency squared (Equation (32)), the acceleration FRF shows the highest peak for the sixth mode. If the sizes of the plate have an order of magnitude of 1 m, they are much smaller than the typical length scale of wind turbulence that excites buildings [31]; therefore, pressure can be considered spatially uniform. For pressure fluctuations related to turbulence having smaller length scales, the possible excitation of higher-order modes has to be evaluated using more sophisticated methods like the acceptance integral [33]; nevertheless, also in this case, the first mode is the most excited [33]. In many practical conditions, the plates can be excited by vibrations coming from the supports [34]; also in this case, the lower-order modes are the most excited.

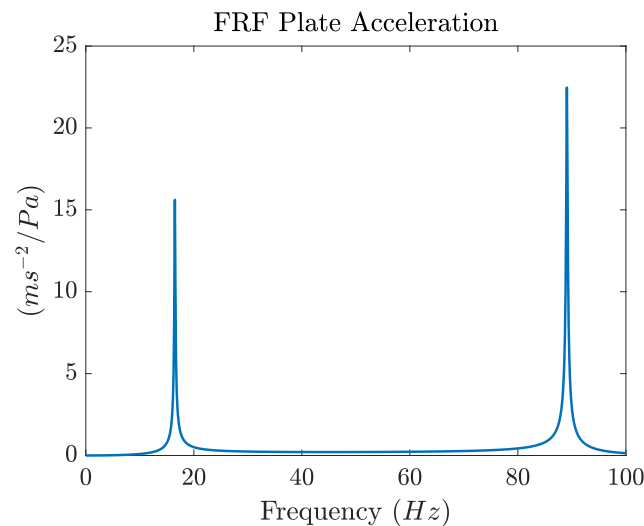


**Figure 4.** The FRF (magnitude) between the acceleration at the center of the plate and the uniform distributed load.

For the above-mentioned reasons, this research focuses on vibration energy harvesting from the first mode of vibration of the plate, and the CPDVA is tuned to the natural frequency of this mode and is located at the center of the plate, which is an anti-node for the first mode of vibration. The mathematical model of the CPDVA is developed starting from the properties of a commercial cantilever harvester M2814P2C-01 built by Smart Material. This harvester has a piezoelectric layer made of macro fiber composite [35] and has a structural layer made of glass fiber composite (FR4). Its properties are summarized in Table 3. The transfer function of the M2814P2C-01 was experimentally evaluated with the impulsive method [36] and showed a resonance peak at 146.69 Hz. Therefore, the addition of a large tip mass is needed to tune the harvester to the first natural frequency of the plate (16.5 Hz).

**Table 3.** Parameters of the M2814P2C-01 cantilever harvester.

Parameter	Value
Structural layer length	70 mm
Structural layer thickness	1 mm
Structural layer width	25 mm
Structural layer elastic modulus	24 GPa
Structural layer density	1920 kg m <sup>-3</sup>
Piezoelectric patch length	28 mm
Piezoelectric patch thickness	0.18 mm
Piezoelectric patch width	14 mm
Piezoelectric patch elastic modulus	30.24 GPa
Piezoelectric patch density	7400 kg m <sup>-3</sup>
Piezoelectric patch capacitance	30.8 nF
Piezoelectric constant $e_{31}$	5.02 pC m <sup>-2</sup>

A small clamp is needed to fix the cantilever base to the plate. If the clamp is made of polymeric material, its mass is about 0.018 kg. Before tuning the harvester to the plate, the effect of the mass of the clamp on the natural frequency of the first plate mode was evaluated by means of the mathematical model of Section 2, setting  $M = 0$  kg. The clamp mass has a very small effect on the natural frequency of the first mode, which moves from 16.5 Hz to 16.4 Hz. Harvester tuning is then carried out by means of Equation (9) by setting the term on the right-hand side to zero (free vibration analysis). The undamped natural frequency is given by:

$$\omega_n = \sqrt{K/M} \quad (37)$$

where  $K$  and  $M$  are given by Equations (13) and (14), respectively. Since all the terms in the expressions of  $K$  and  $M$  are known except  $M_t$ , the undamped natural frequency ( $\omega_n$ ) is set equal to the natural frequency of the first mode of the plate, and the tip mass that tunes the harvester is found: the calculated value is  $M_t = 0.051$  kg.

The calculations reported in this section aim to show the validity of the CPDVA and the importance of tuning and the location of the device. The focus is on voltage generation. Figure 5 makes a comparison between the acceleration FRF at the center of the plate and the acceleration FRF at the same point when the CPDVA is tuned to the first mode of the plate and is mounted at the center of the plate. Since the dimensions of the patch are very small compared to the dimensions of the plate, the effect of the patch is negligible, and simulations show that the difference between the first natural frequency calculated with and without the patch is about  $3 \times 10^{-3}$  Hz. To calculate the FRFs, a distributed load with constant amplitude and variable frequency ( $q_z(t)$ ) is assumed to excite the plate.

As in the other cases considered in the scientific literature (e.g., beams [22]), the CPDVA eliminates the original resonance peak of the plate and generates a couple of new peaks: the first at a lower frequency and the second at a higher frequency. The amplitudes of the new acceleration peaks are significantly lower than the one of the original resonance peak of the bare plate. Figure 6 makes a comparison between the OC voltage FRF of the CPDVA tuned to the first mode of the plate and mounted at the center of the plate and the OC voltage FRF of a piezoelectric patch directly bonded under the center of the plate. The first mode of the plate corresponds to the bending of a beam in the  $x$ - $z$  plane; hence, when the first mode is excited, the curvature at the center of the plate is large and the electro-mechanical coupling between the patch and the plate is large. Indeed, for the first mode, Equation (16) can be generalized for the patch bonded on the plate as:

$$\theta = -e_{3,1} b_p h_{pcp} \int_{x_1}^{x_2} \frac{\partial^2 \Phi_1}{\partial x^2} dx \quad (38)$$

where  $h_{pcp}$  is the distance between the center of the piezoelectric layer and the neutral axis of the plate, and  $x_1, x_2$  are the coordinates of the extremities of the patch. This piezoelectric patch has the same properties and sizes of the piezoelectric layer included in the M2814P2C-01 harvester. Figure 6 highlights that the CPDVA generates much more voltage than the patch because not only are the two peaks of CPDVA higher than the peak of the patch, but also, the bandwidths around resonances are larger. The latter effect can be very useful in the presence of broadband random excitation.

In the previous simulations, the CPDVA was mounted at the center of the plate ( $x_a = a/2$   $y_a = b/2$ ), where the first mode of vibration shows the largest amplitudes (see Figure 2). In the simulations reported in Figure 7, the CPDVA is moved from the best location along the longitudinal direction ( $x$ ). It is worth noting that since the first mode of the plate is symmetric, leftward and rightward displacements have the same effect on the coupling between the CPDVA and this mode of the plate. A harmonic distributed load with constant amplitude and variable frequency ( $q_z(t)$ ) is assumed to excite the plate.

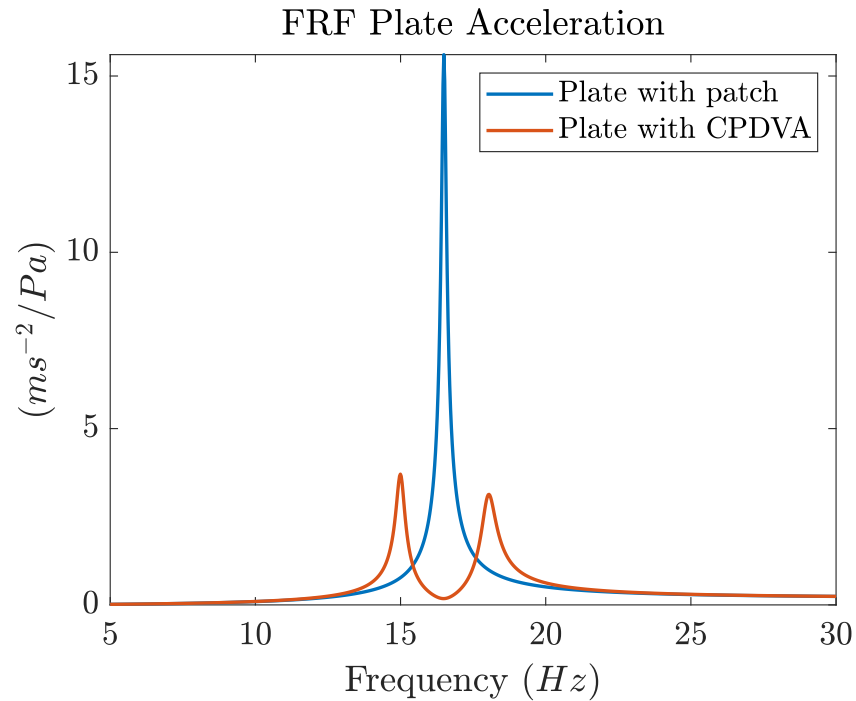


**Figure 5.** Comparison between the magnitude of calculated FRF of the acceleration at the center of the plate and the uniformly distributed load: plate with patch and plate with CPDVA.

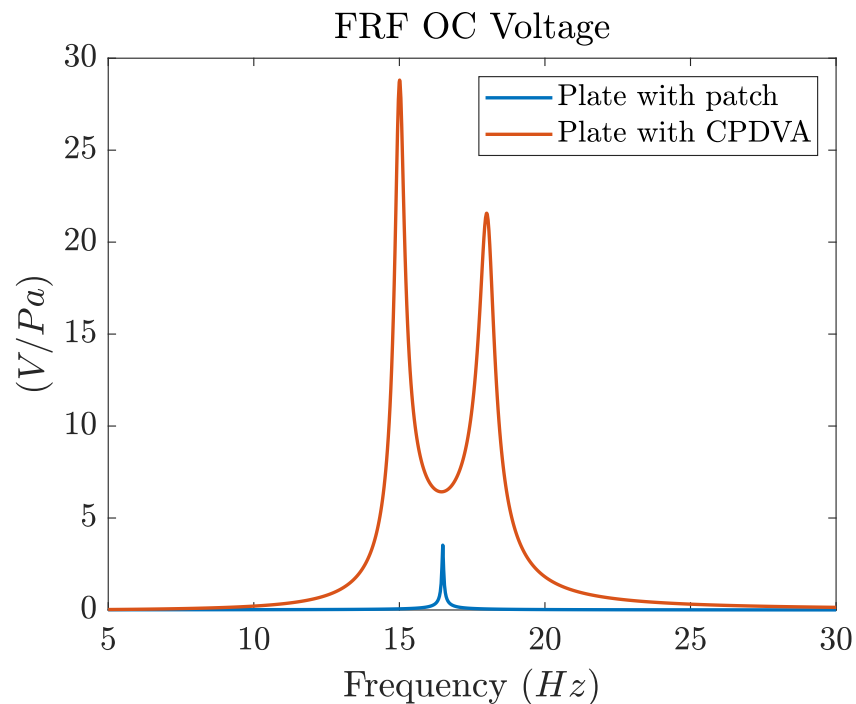


**Figure 6.** Comparison between the magnitude of calculated FRF of the generated OC voltage and the uniformly distributed load: plate with patch and plate with CPDVA.

The FRF between the acceleration of the point of the plate just above the CPDVA and the distributed load shows that the coupling between the CPDVA and the plate decreases when the CPDVA is moved from the center of the plate, i.e., when  $x_a < a/2$ . Indeed, the peaks of the FRF become closer and their amplitudes decrease. Eventually, when the CPDVA is located near the nodal line, the two peaks tend to merge into a unique peak.

The FRF between the generated OC voltage and the distributed load shows that the bandwidth that includes the two resonance peaks decreases when the CPDVA is moved from the central position. This is a negative effect when the plate is excited by broadband random pressure fluctuations. The effect of the CPDVA position on the peaks of the OC voltage FRF is more complex. If the lateral displacement is small (e.g.,  $x_a = a/4$ ), the amplitudes of the two peaks decrease. The maximum amplitude is reached when the two peaks merge into a unique peak ( $x_a = a/10$ ). Eventually, peak amplitude decreases when the CPDVA is close to the nodal line of the plate mode. This behavior can be exploited if the plate is excited by a harmonic load having a well-defined frequency.

In Figure 8, the CPDVA is moved from the center of the plate in the lateral direction ( $y$ ). This displacement does not affect the coupling with the first mode of vibration of the plate and with the other modes for which  $n = 0$  (see Table 2 and Figure 2), but it alters the coupling with the modes with  $n \neq 0$ , e.g., the second mode. Therefore, this effect can be found only when the CPDVA is coupled with a plate. The FRF between the acceleration of the plate point above the CPDVA and the distributed load shows small modifications in the position and height of the two main resonance peaks, but when the CPDVA is moved towards the anti-node of the second mode ( $y_a = 0$ ), a minor resonance peak at the frequency of the second peak appears. This phenomenon happens because when  $y_a$  decreases, there is coupling between the CPDVA and the second mode as well. Since this coupling alters the shape of the second mode, the uniformly distributed load is able to cause a small excitation of the second mode. The excitation of the second mode slightly alters the effect of the CPDVA on the first mode, and the OC voltage FRF shows small variations in the position and height of the main resonance peaks. For  $x_a = a/2$ ,  $y_a = 0$ , the second peak becomes higher.

Figure 9 deals with the effect of CPDVA tuning; in this case, the harvester is always at the center of the plate, which is excited by a harmonic distributed load ( $q_z(t)$ ).

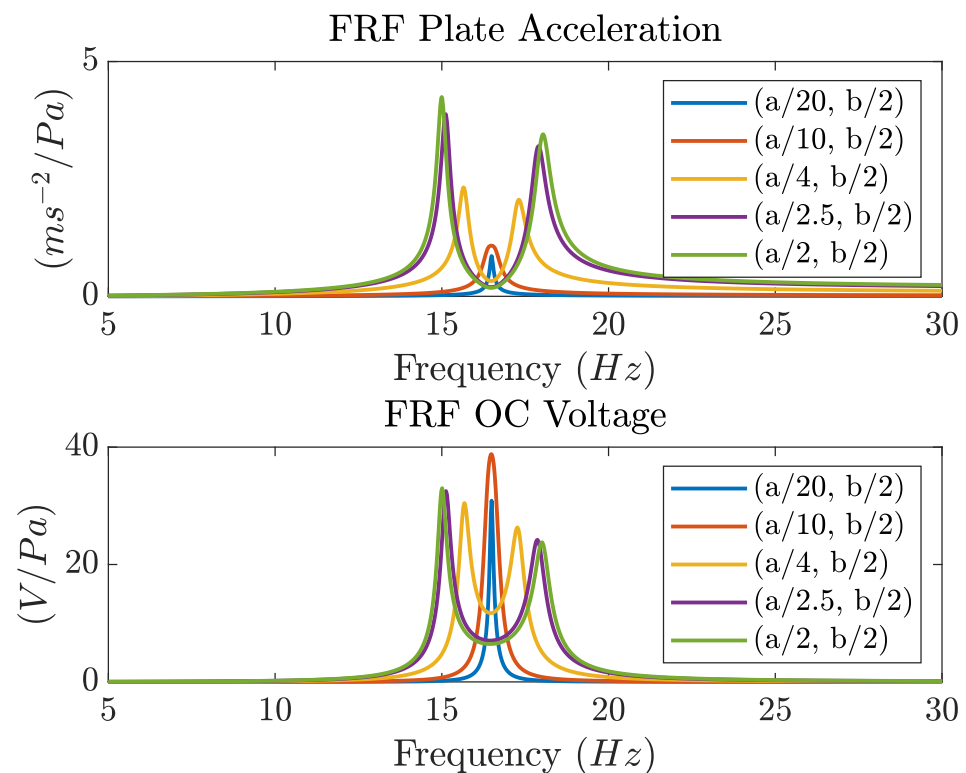


**Figure 7.** FRF (magnitude) of the acceleration at the center of the plate (**top**) and FRF of the OC voltage generated by the CPDVA (**bottom**). Comparison considering different positions of the harvester along the x-axis (and the same position along the y-axis) and the uniformly distributed load.

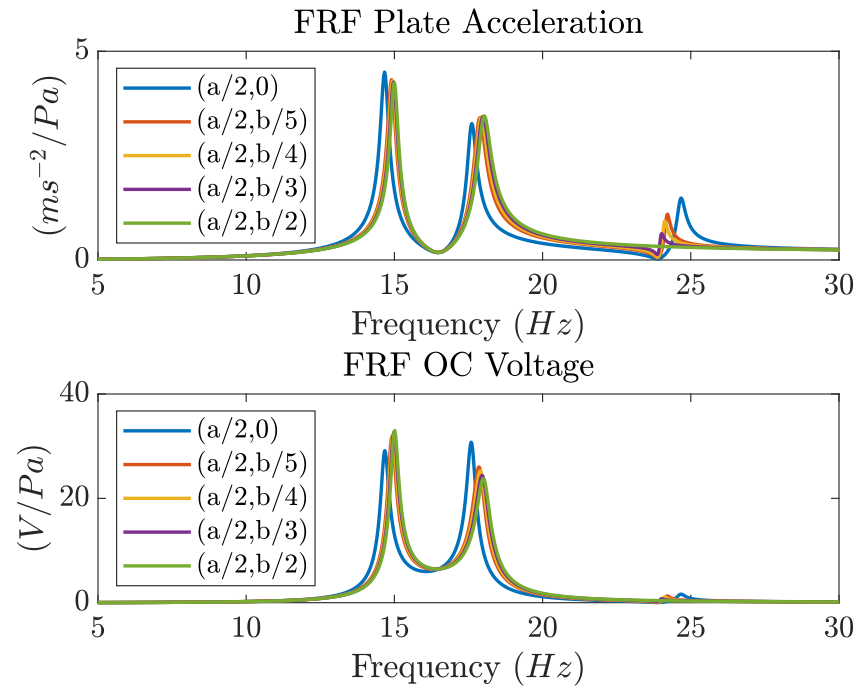


**Figure 8.** FRF (magnitude) of the acceleration at the center of the plate (**top**) and FRF of the OC voltage generated by the CPDVA (**bottom**). Comparison considering different positions of the harvester along the y-axis (and the same position along the x-axis) and the uniformly distributed load.

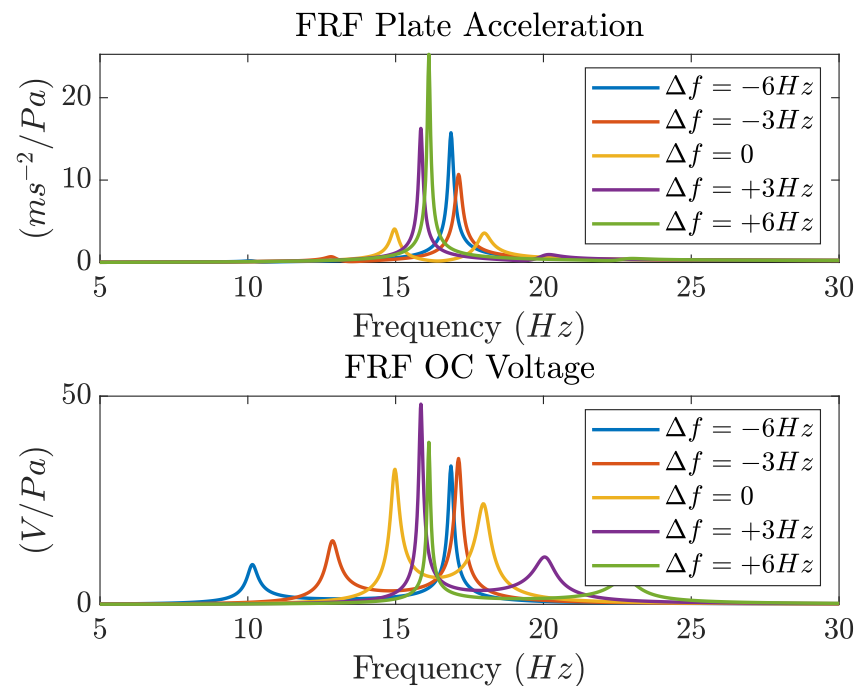


**Figure 9.** FRF (magnitude) of the acceleration at the center of the plate (**top**) and FRF of the OC voltage generated by the CPDVA (**bottom**). Comparison considering different tuning frequencies of the harvester and the uniformly distributed load.

The maximum effect on plate acceleration takes place when the CPDVA is tuned to the natural frequency of the first mode of the plate. This behavior is typical of many vibrating systems [22]. A shift in the tuning frequency  $\Delta f = 3$  Hz (about 20%) is enough to make a large resonance peak appear again. The frequency of this resonance is close to the one of the original resonance of the plate and depends on CPDVA tuning.

Figure 9 shows that all of the OC voltage FRFs intersect at the frequency of the original mode of the plate (16.5 Hz). Exact tuning leads to the most-symmetric behavior, with two peaks of the OC voltage having nearly the same amplitude and the minimum being at the natural frequency of the original plate mode.

If the tuning frequency is shifted from the value corresponding to the natural frequency of the first mode, the maximum peak of the voltage FRF always coincides with the maximum peak of the acceleration FRF. When the tuning frequency decreases, the first peak moves to lower frequencies and decreases its amplitude, whereas the second peak moves towards the natural frequency of the plate, increases, and eventually decreases when  $\Delta f = -6$  Hz. In a simply supported beam forced by a concentrated load and equipped with a cantilever DVA, similar behavior was found when the value of the tuning mass was increased (tuning frequency decreased) [22]. When the tuning frequency increases, the second peak moves to higher frequencies, whereas the first moves towards the original natural frequency of the plate, increases, and eventually decreases when  $\Delta f = -6$  Hz. The behavior is not symmetric since positive and negative frequency shifts have different effects. The behavior depicted in Figure 9 suggests that when the distributed load has a broadband spectrum, the best tuning coincides with the exact tuning to the natural frequency of the plate mode. When a narrow-band distributed load excites the plate, the largest amount of energy can be harvested when the harvester is tuned to a slightly higher frequency.

#### 4. Experimental Equipment

The experimental tests were performed in the Laboratory of Vibration Mechanics of Padova University in the absence of ambient vibrations and wind.

The experimental equipment was developed with the aim of evaluating the performance of the harvesting system in different load conditions. To make the clamps, the two shorter sides of the aluminum plate were fixed to a very stiff steel base by means of screws (Figure 10). The CPDVA used in experiments was built using a commercial cantilever harvester (PEH M2814P2C-01) made by Smart Materials GmbH. The base to attach the harvester to the plate was 3D printed using polylactide (PLA) filament. Table 3 reports the parameters of the harvester, and Figure 11 shows the CPDVA attached to the backside of the plate. The CPDVA base was bonded to the center of the plate ( $x = a/2$ ,  $y = b/2$ ) by means of structural adhesive.

In order to verify the advantages of the CPDVA, experiments were also performed with a piezoelectric patch in place of the CPDVA. In particular, the same piezoelectric patch used in the PEH M2814P2C-01 cantilever harvester was bonded under the center of the plate, as shown in Figure 12. The piezoelectric patch was bonded with the piezoelectric patch length oriented along the  $x$ -axis of the plate. The patch was bonded with an offset of 5 cm in the  $y$ -axis with respect to the center of the plate, whereas no offset was used in the  $x$  direction. Since the first mode of vibration is predominant, this offset does not affect the results much.

During tests, the OC voltage generated by the piezoelectric layer and the acceleration of the center of the plate were measured. The latter measurement was carried out using a small PCB 352C22 accelerometer (sensitivity 10.48 mV/g, measurement range  $\pm 4900$  m/s<sup>2</sup> and frequency range 1.0 to 1000 Hz), which was attached by means of wax. Since the mass of this accelerometer is less than 1 g (value from datasheet:  $5 \times 10^{-4}$  kg), it does not affect the dynamics of the plate.

Two load cases were considered in the framework of this research. In the first, the center of the plate was excited by means of a hammer for modal testing PCB 086C03 (sensitivity 2.25 mV/N, measurement range  $\pm 2224$  N and hammer mass 0.16 kg). Since in this case, measurement of the exciting force was possible and reliable, the FRFs of the system were calculated. It is worth noting that the simulations presented in Section 3 show that there are small differences between the general trend of the FRFs obtained with uniform pressure load and the FRFs obtained with concentrated force acting at the center of the plate (e.g., compare Figure 6 to figures of Section 5.1).



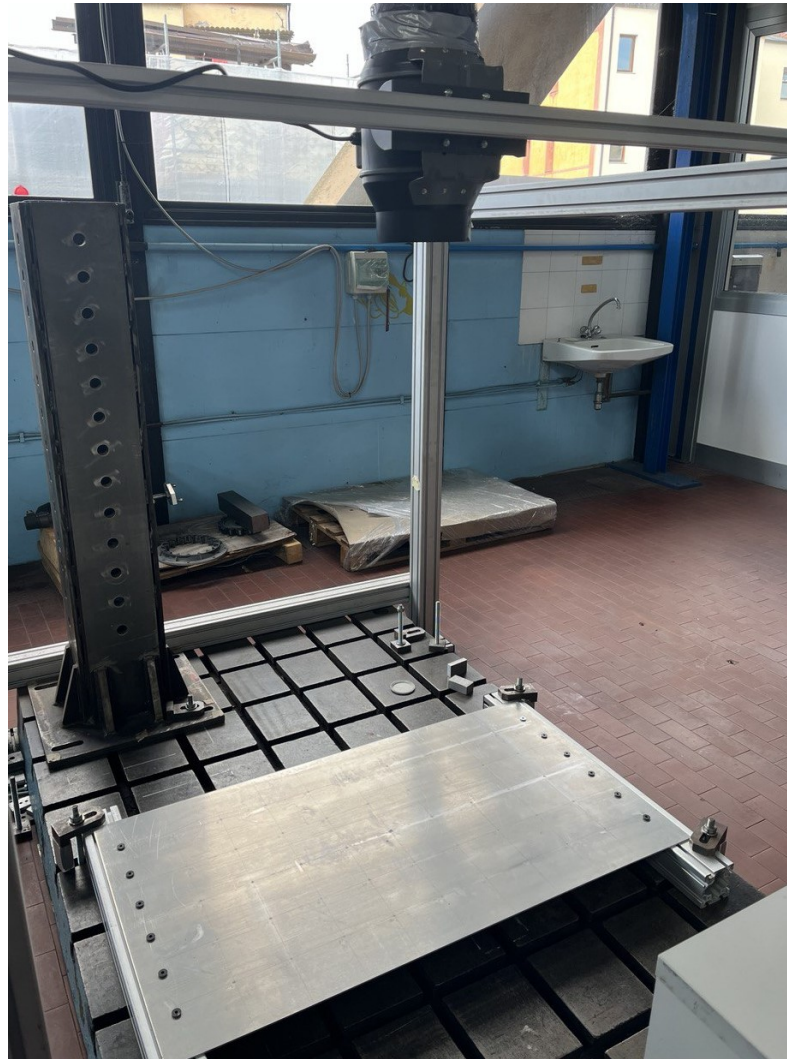


**Figure 10.** Clamped plate and fan for excitation of the plate via air jet.

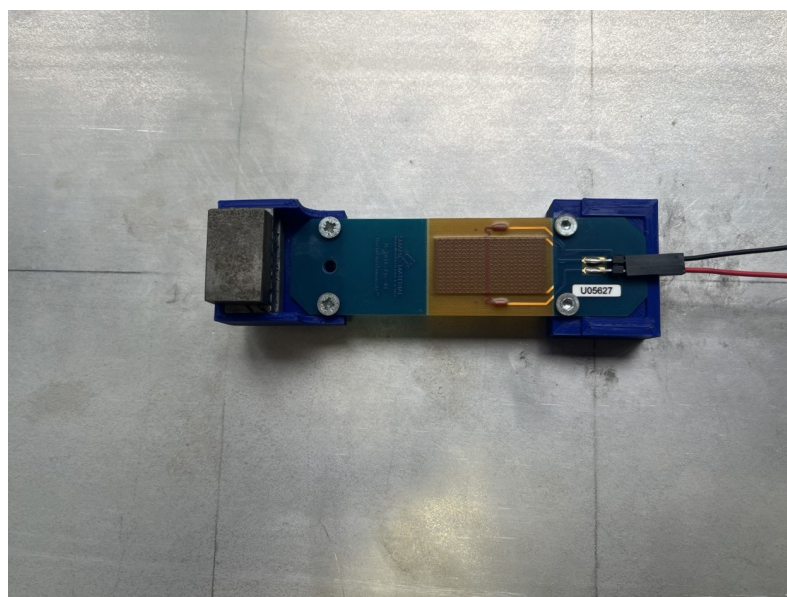


**Figure 11.** Picture of the CPDVA. The tip mass is on the left-hand side, and the base glued to the plate is on the right-hand side.

In the second load case, a fan was installed over the plate at a distance of 1.2 m, see Figure 10. The plate was excited by the pressure generated by the air jet impinging on the plate surface. The fan diameter is 0.148 m, and the maximum flow rate is 595 m<sup>3</sup>/h, which corresponds to a Reynolds number  $Re \approx 10^5$ . Experimental tests dealing with turbulent jets impinging on flat surfaces were presented in [37–39]. The results show axial-symmetric distributions of both mean velocities and fluctuating components, which reach maximum values at small distances from the jet axis: that is, at the center of the plate. The pressure fluctuations caused by the above-mentioned pressure distributions can excite the first mode of the plate but cannot excite the modes with an odd number of nodal lines.

The voltage generated by the CPDVA and the signals of the sensors were acquired through an NI9230 board. Measurements were performed in the range 0 ÷ 1024 Hz, and typically, 4096 samples were collected, with a sampling frequency of 2048 Hz. Then, the digital signals were analyzed with the software NI Signal Express to obtain the FRFs between voltage, acceleration and force and the PSDs of the OC voltage.



**Figure 12.** Piezoelectric patch directly bonded to the plate.

## 5. Experimental Results

### 5.1. Tests with Impulsive Excitation

A preliminary experimental modal analysis of the clamped plate was carried out to check the natural frequencies and the modal shapes. Good agreement with analytical results was found. Since the experimental natural frequency of the first mode was slightly lower than the analytical value, the tip mass was increased ( $M_t = 0.058$  kg); the resulting total mass of the CPDVA was 0.119 kg.

For the load case with impulsive excitation, the plate equipped with the CPDVA and the accelerometer was excited through the hammer for modal testing. Even though the hammer hits were exerted by a well-trained operator, there were small errors in the position and orientation of the impulsive force. Hence, to improve the reliability of measurements, the test was repeated seven times. Figure 13 shows the impulsive force applied by the hammer and the measured acceleration and voltage. As shown by experimental data, applying this type of excitation gives good repeatability of the results. The presence of beats in the signal of the voltage generated by the CPDVA highlights the presence of two close natural frequencies in the system.

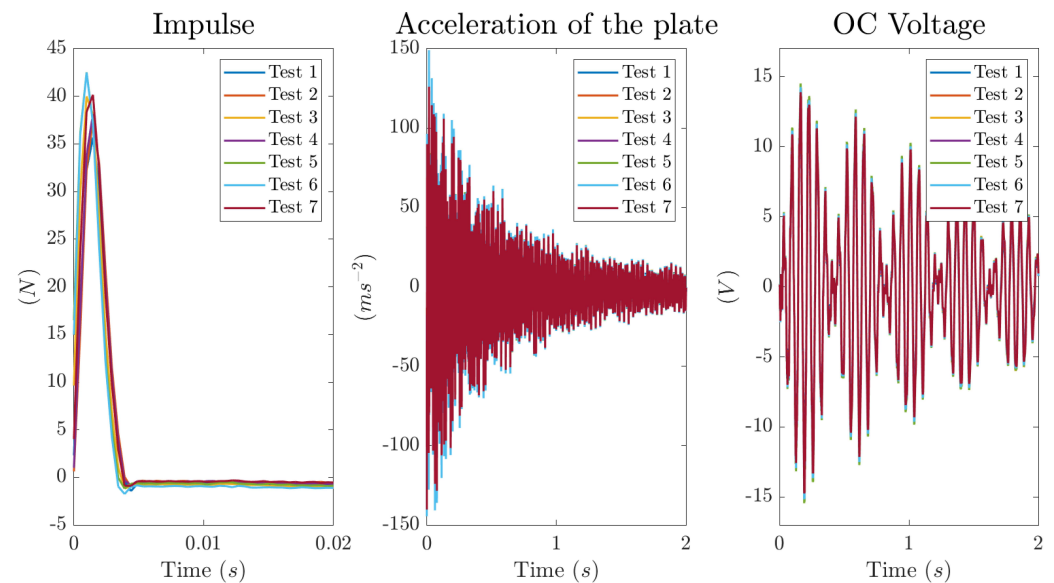


**Figure 13.** Experimental results obtained by means of an impulse applied at the center of the plate with CPDVA: impulse (left), acceleration at the center of the plate (center) and OC voltage generated by the CPDVA (right).

The measured data were elaborated to retrieve (1) the FRF between the acceleration at the center of the plate and the concentrated load applied to the center of the plate and (2) the FRF between the OC voltage and the concentrated load applied to the center of the plate. The magnitudes of these FRFs are shown in Figure 14 together with the magnitudes of the FRFs predicted by the mathematical model.

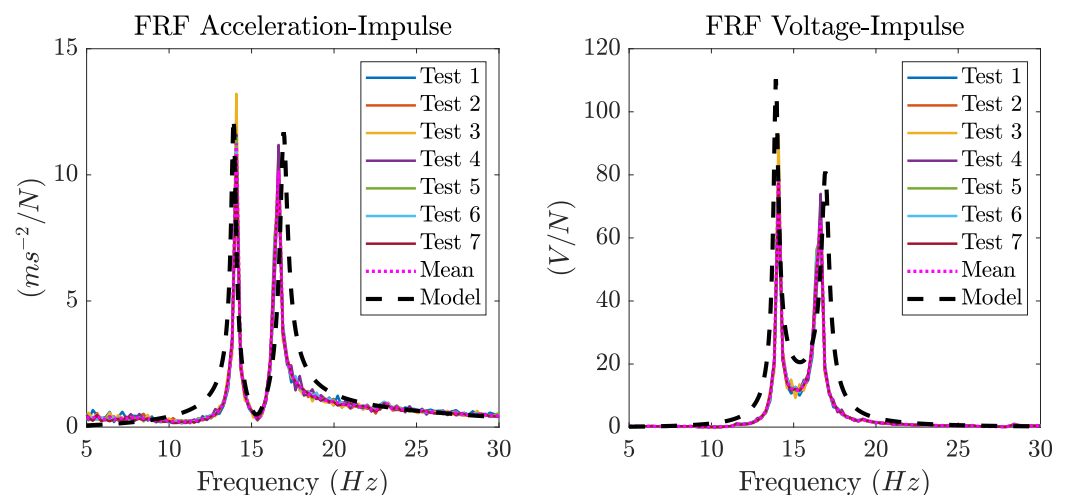


**Figure 14.** Magnitude of the FRF between the acceleration at the center of the plate and the impulse (left) and magnitude of the FRF between the the OC voltage generated by the CPDVA and the impulse (right). Experimental and predicted FRFs for the impulse applied to the center of the plate.

As expected, the original resonance peak of the plate (15.4 Hz) is eliminated by the CPDVA, and a couple of new peaks are generated: the first at a lower frequency (14.0 Hz) and the second at a higher frequency (16.9 Hz). The presence of the two peaks in the voltage FRF enables energy harvesting in a broad frequency band; this is useful in the case of random excitation. The curves for the different tests are very similar.

There is good agreement between the general trend of the experimental FRFs and the FRFs predicted by the mathematical model with concentrated load excitation (Section 2). In particular, the mathematical model predicts the frequencies of the new peaks with an error

smaller than 0.5 Hz. The mathematical model slightly overestimates the amplitudes of the peaks of the acceleration FRF when compared with the mean experimental values. Similar behavior is found when the amplitudes of the peaks of the voltage FRF are compared with the mean experimental values, but in this case, the overestimation increases. These differences in the amplitudes can be due to uncertainties in the identification of the damping coefficient of the harvester.

In order to evaluate the performance of the CPDVA, the tests with hammer excitation were repeated, substituting the CPDVA with the piezoelectric patch bonded to the plate. Measured acceleration and voltage generated by the simple patch are shown in Figure 15, and the amplitudes of the FRFs obtained from these measures are shown in Figure 16.

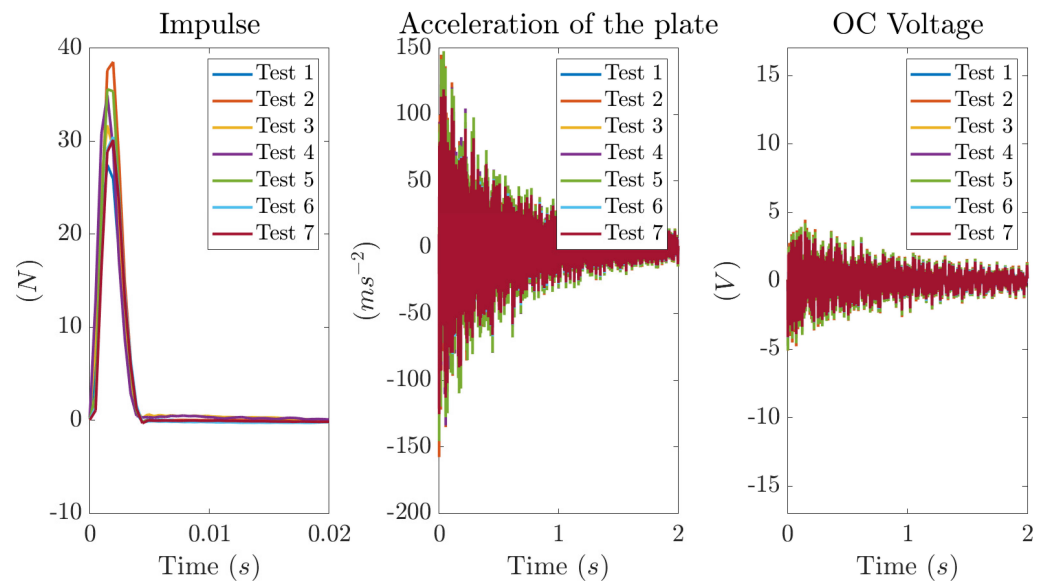


**Figure 15.** Experimental results obtained by means of an impulse applied at the center of the plate with the piezoelectric patch directly bonded to the plate: impulse (left), acceleration at the center of the plate (center) and OC voltage generated by the patch (right).

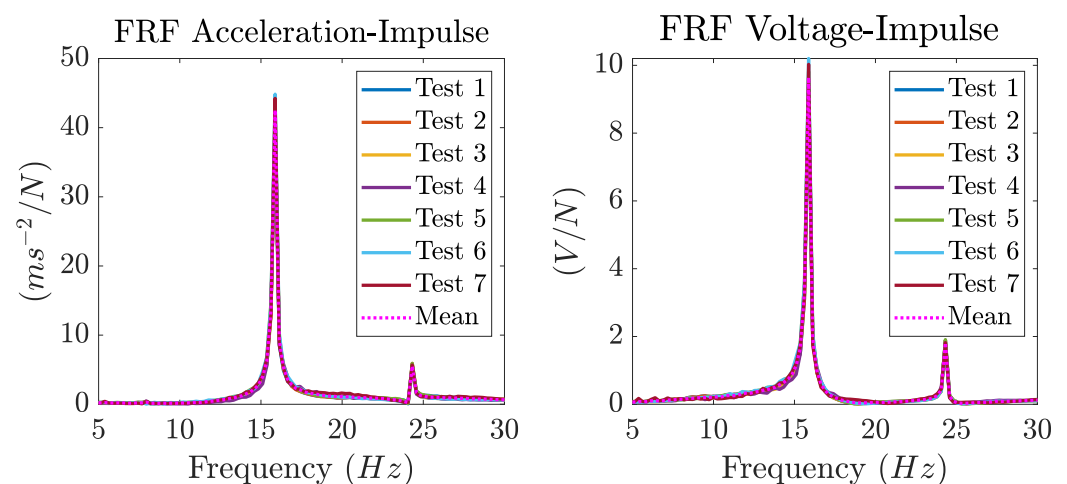


**Figure 16.** Magnitude of the FRF between the acceleration at the center of the plate and the impulse (left) and the magnitude of the FRF between the OC voltage generated by the piezoelectric patch bonded to the plate and the impulse (right). Experimental and predicted FRFs for the impulse applied to the center of the plate.

Analysis of time-domain data shows that the maximum voltage generated by the patch is about three times smaller than the maximum voltage generated by the CPDVA and very quickly reaches values lower than  $\pm 1$  V. The experimental FRFs show the highest



peaks at the first natural frequency of the plate. The height of the peak of the voltage FRF obtained with the patch is one order of magnitude smaller than the peaks obtained with the CPDVA. In order to quantify the performance of the patch and of the CPDVA, the root mean square value (RMS) of the OC voltage was calculated for each test, and then, the mean RMSs of both harvesting systems were calculated. In particular, the mean RMSs of the OC voltage generated by the patch and by the CPDVA are 0.75 V and 3.86 V, respectively.

In Figure 16, a small peak corresponding to the second natural frequency of the plate can be observed. Indeed, the patch was bonded with an offset in the y direction with respect to the center of the plate. Moreover, the hammer hit was manually generated and was not exactly centered nor aligned to be perpendicular to the plate. Thus, it was able to weakly excite the second mode of the plate.

Finally, the robustness of CPDVA was assessed by carrying out experimental tests using a CPDVA with a small tuning error  $\Delta f \approx -1$  Hz. The results, which are reported in Figure 17, show some modification to the OC voltage FRF that do not decrease the effectiveness of the vibration harvesting system. In particular, the two peaks move to lower frequencies (13.31 Hz and 16.13 Hz, respectively). The amplitude of the first peak decreases, whereas the amplitude of the second peak increases and becomes larger than the amplitude of the first peak. These results are in agreement with the calculated results of Section 3 (which refer to a uniformly distributed load).

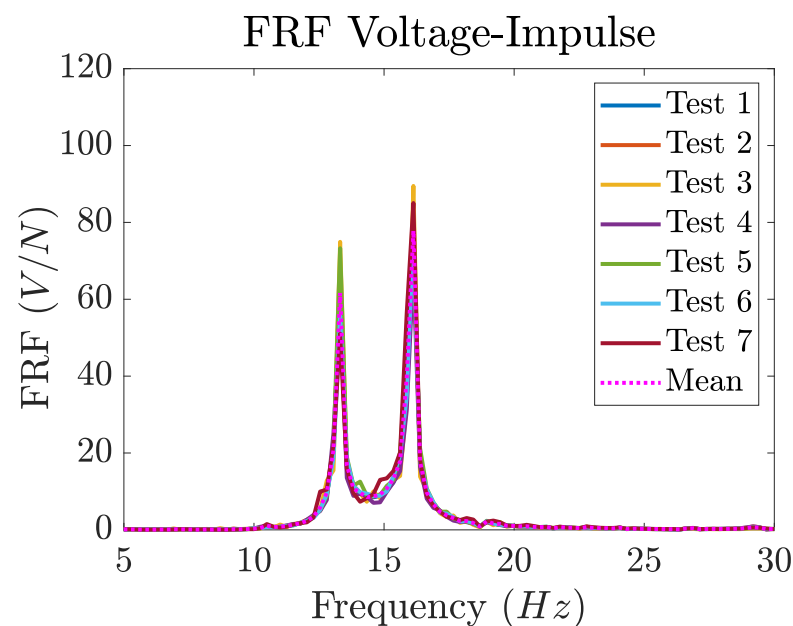


**Figure 17.** Magnitude of the FRF between the OC voltage and the impulse in the presence of tuning error  $\Delta f \approx -1$  Hz.

## 5.2. Tests with Air Excitation

The fan depicted in Figure 10 was used to excite the plate by means of random pressure oscillations. Several tests were carried out with air velocities ranging from 4.1 to 9.0 m/s (the maximum value corresponds to the maximum flow rate of the fan). In the first series of tests, the simple piezoelectric patch was bonded under the center of the plate, whereas in the second series of tests, the CPDVA was fixed under the center of the plate. The OC voltage generated by the piezoelectric layer was analyzed in the frequency domain by means of NI Signal Express to obtain the power spectral density (PSD). In every test condition, the test was repeated seven times and good repeatability was found. Figure 18 refers to the voltage generated by the patch. The voltage PSD shows a peak at the natural frequency of the first mode of the plate. The height of this peak strongly increases with air velocity and reaches the maximum value of about 0.02 V<sup>2</sup>/Hz when the air velocity is 9.0 m/s. It is worth noting that at the maximum air velocity, a minor peak at the natural frequency of

the second mode of the plate appears as well. Since the air flow is able to strongly excite only the first mode of vibration of the plate, pressure fluctuations generated by the air flow can be considered to be spatially uniform on the plate surface and are dominated by low frequency components, as happens in the excitation of buildings by wind.

Figure 19 shows the PSD of OC voltage generated by the CPDVA. Also, in this case, the generated voltage strongly increases with air velocity, but amplitudes are much larger than the ones in the previous case, with peaks ranging from 0.5 to 1  $V^2/Hz$  when air velocity reaches the maximum value. The effect of the CPDVA is clearly shown by the presence of the two peaks around the frequency of the first mode of the plate: like in the impulsive tests, the first peak is higher.

### PSD OC Voltage

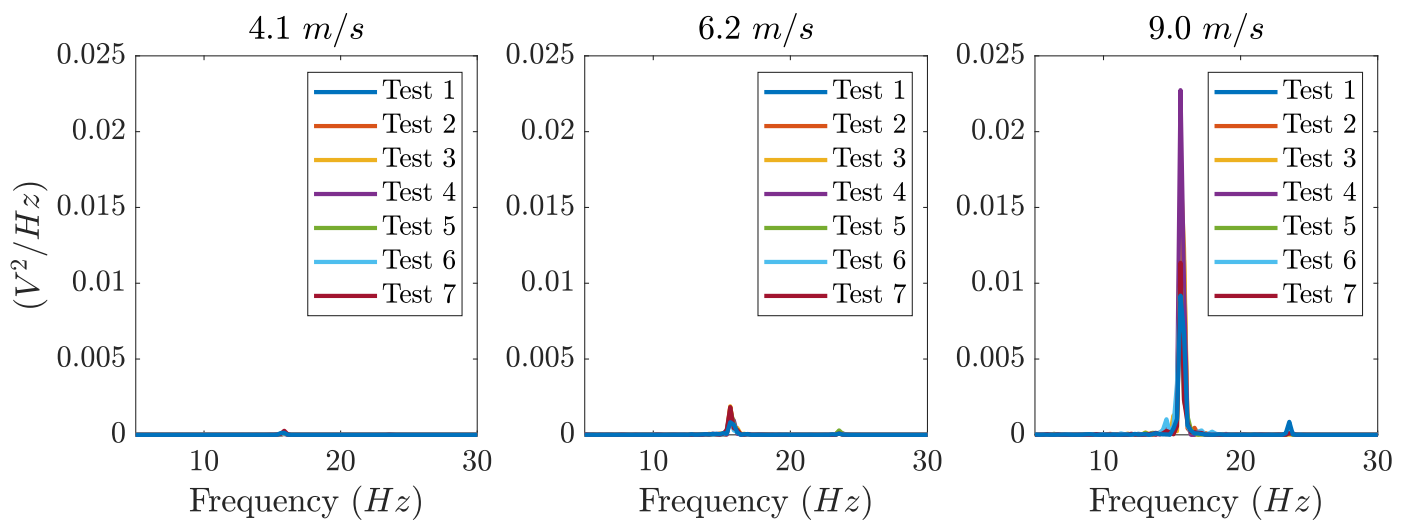


**Figure 18.** PSD of the OC voltage generated by the patch directly bonded on the plate excited by the air jet. Experimental results are reported for three values of air velocity.

### PSD OC Voltage

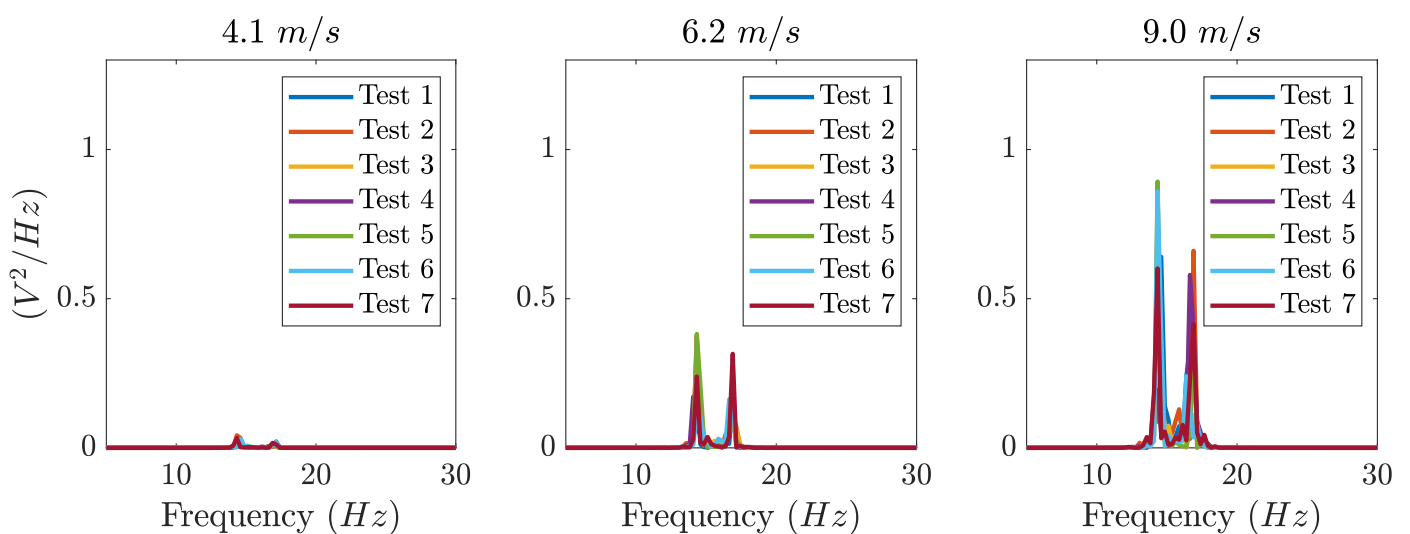


**Figure 19.** PSD of the OC voltage generated by the CPDVA excited by the air jet. Experimental results are reported for three values of air velocity.

## 6. Conclusions

In many conditions relevant to industrial and civil applications, the response of a vibrating plate is dominated by the first mode of vibration as it has the lowest natural frequency and the simplest modal shape. Direct energy harvesting from plate vibrations by means of a piezoelectric patch bonded to the plate is not very efficient since the plate is stiff and the strain is small. The CPDVA transfers the vibration energy of the plate to the small cantilever of the harvester, which has a less stiff section (made of piezoelectric and plastic materials); hence, the generation of voltage is strongly enhanced. This result is confirmed both by simulations and by experimental tests carried out with impulsive excitation and air excitation. The RMSs of the OC voltage generated by the piezoelectric patch and by the CPDVA were calculated. The RMS of the OC voltage generated by the CPDVA is about five times larger than the one generated by the patch.

In the presence of broadband excitation that includes both of the peaks generated by the CPDVA, experimental and calculated results show that the optimal configuration includes a CPDVA that is exactly tuned to the first natural frequency of the plate and is mounted at the center of the plate (which is a vibration anti-node for the first mode).

Simulations showed that the harvester's performance is affected by location and tuning; nevertheless, the system is rather robust, and small variations in tuning and location do not have a large effect on the peaks of the FRF and, hence, on the generated voltage. Conversely, large variations in harvester position or tuning strongly modify the peaks of the FRF, and this effect can be exploited to optimize the harvester in the presence of specific loads: wind and rain loads, loads generated by traffic and narrow-band excitation due to machine unbalance.

Possible future developments include the application of CPDVA to solar panels in order to develop a hybrid solar–vibration harvesting system able to generate energy even in adverse weather conditions.

**Author Contributions:** Conceptualization, M.T., A.P. and A.D.; methodology, M.T., A.P. and A.D.; software, M.T. and A.P.; validation, M.T., A.P. and A.D.; formal analysis, M.T., A.P. and A.D.; investigation, M.T., A.P. and A.D.; writing—original draft preparation, M.T., A.P. and A.D.; writing—review and editing, M.T., A.P. and A.D.; supervision, A.D. All authors have read and agreed to the published version of the manuscript.

**Funding:** This research received no external funding.

**Institutional Review Board Statement:** Not applicable.

**Informed Consent Statement:** Not applicable.

**Data Availability Statement:** Data are contained within the article.

**Conflicts of Interest:** The authors declare no conflicts of interest.

## References

1. Erturk, A.; Inman, D.J. On mechanical modeling of cantilevered piezoelectric vibration energy harvesters. *J. Intell. Mater. Syst. Struct.* **2008**, *19*, 1311–1325. [\[CrossRef\]](#)
2. Xie, Z.; Teng, L.; Wang, H.; Liu, Y.; Fu, M.; Liang, J. A Self-Powered Synchronous Switch Energy Extraction Circuit for Electromagnetic Energy Harvesting Enhancement. *IEEE Trans. Power Electron.* **2023**, *38*, 9972–9982. [\[CrossRef\]](#)
3. Chen, L.; Ma, Y.; Hou, C.; Su, X.; Li, H. Modeling and analysis of dual modules cantilever-based electrostatic energy harvester with stoppers. *Appl. Math. Model.* **2023**, *116*, 350–371. [\[CrossRef\]](#)
4. Ye, C.; Liu, D.; Chen, P.; Cao, L.N.; Li, X.; Jiang, T.; Wang, Z.L. An Integrated Solar Panel with a Triboelectric Nanogenerator Array for Synergistic Harvesting of Raindrop and Solar Energy. *Adv. Mater.* **2023**, *35*, 2209713. [\[CrossRef\]](#)
5. Jiao, P.; Nazar, A.M.; Egbe, K.J.I.; Rayegani, A. Magnetically circular layers triboelectric nanogenerators (MCL-TENG) for velocity sensing and damage detection. *Sustain. Energy Technol. Assess.* **2022**, *53*, 102644. [\[CrossRef\]](#)
6. Warburton, G. The vibration of rectangular plates. *Proc. Inst. Mech. Eng.* **1954**, *168*, 371–384. [\[CrossRef\]](#)
7. Tommasino, D.; Moro, F.; Zumalde, E.; Kunzmann, J.; Doria, A. An Analytical–Numerical Method for Simulating the Performance of Piezoelectric Harvesters Mounted on Wing Slats. *Actuators* **2023**, *12*, 29. [\[CrossRef\]](#)
8. Bedon, C.; Fasan, M.; Amadio, C. Vibration Analysis and Dynamic Characterization of Structural Glass Elements with Different Restraints Based on Operational Modal Analysis. *Buildings* **2019**, *9*, 13. [\[CrossRef\]](#)



9. Pipitone, G.; Barone, G.; Palmeri, A. Optimal design of double-skin façades as vibration absorbers. *Struct. Control Health Monit.* **2018**, *25*, e2086. [\[CrossRef\]](#)
10. Priya, S.; Inman, D.J. *Energy Harvesting Technologies*; Springer: Berlin/Heidelberg, Germany, 2009; Volume 21.
11. Thorby, D. *Structural Dynamics and Vibration in Practice*; Elsevier Ltd.: Amsterdam, The Netherlands, 2008.
12. Aldraihem, O.; Baz, A. Energy harvester with a dynamic magnifier. *J. Intell. Mater. Syst. Struct.* **2011**, *22*, 521–530. [\[CrossRef\]](#)
13. Aladwani, A.; Arafa, M.; Aldraihem, O.; Baz, A. Cantilevered Piezoelectric Energy Harvester With a Dynamic Magnifier. *J. Vib. Acoust.* **2012**, *134*, 031004. [\[CrossRef\]](#)
14. Zhou, W.; Penamalli, G.R.; Zuo, L. An efficient vibration energy harvester with a multi-mode dynamic magnifier. *Smart Mater. Struct.* **2011**, *21*, 015014. [\[CrossRef\]](#)
15. Doria, A.; Medè, C.; Fanti, G.; Desideri, D.; Maschio, A.; Moro, F. Development of piezoelectric harvesters with integrated trimming devices. *Appl. Sci.* **2018**, *8*, 557. [\[CrossRef\]](#)
16. Adhikari, S.; Banerjee, A. Enhanced low-frequency vibration energy harvesting with inertial amplifiers. *J. Intell. Mater. Syst. Struct.* **2022**, *33*, 822–838. [\[CrossRef\]](#)
17. Asai, T.; Araki, Y.; Ikago, K. Energy harvesting potential of tuned inertial mass electromagnetic transducers. *Mech. Syst. Signal Process.* **2017**, *84*, 659–672. [\[CrossRef\]](#)
18. Ali, S.F.; Adhikari, S. Energy harvesting dynamic vibration absorbers. *J. Appl. Mech.* **2013**, *80*, 041004. [\[CrossRef\]](#)
19. Abdelmoula, H.; Dai, H.; Abdelkefi, A.; Wang, L. Control of base-excited dynamical systems through piezoelectric energy harvesting absorber. *Smart Mater. Struct.* **2017**, *26*, 095013. [\[CrossRef\]](#)
20. Erturk, A.; Inman, D.J. An experimentally validated bimorph cantilever model for piezoelectric energy harvesting from base excitations. *Smart Mater. Struct.* **2009**, *18*, 025009. [\[CrossRef\]](#)
21. Sulaiman, L.H.; Anuar, M.A.; Zamri, A. An empirical study on the effectiveness of energy harvesting from dynamic vibration absorber. *ARPN J. Eng. Appl. Sci.* **2021**, *16*, 2674–2683.
22. Rezaei, M.; Talebitooti, R.; Liao, W.H. Concurrent energy harvesting and vibration suppression utilizing PZT-based dynamic vibration absorber. *Arch. Appl. Mech.* **2022**, *92*, 363–382. [\[CrossRef\]](#)
23. Rajarathinam, M.; Ali, S.F. Parametric uncertainty and random excitation in energy harvesting dynamic vibration absorber. *ASCE-ASME J. Risk Uncertain. Eng. Syst. Part B Mech. Eng.* **2021**, *7*, 010905. [\[CrossRef\]](#)
24. Rezaei, M.; Talebitooti, R.; Liao, W.H.; Friswell, M.I. Integrating PZT layer with tuned mass damper for simultaneous vibration suppression and energy harvesting considering exciter dynamics: An analytical and experimental study. *J. Sound Vib.* **2023**, *546*, 117413. [\[CrossRef\]](#)
25. Leissa, A.W. *Vibration of Plates*; Scientific and Technical Information Division, NASA headquarters: Washington, DC, USA, 1969; Volume 160.
26. Tommasino, D.; Moro, F.; de Pablo Corona, E.; Vandi, L.; Baietta, A.; Pracucci, A.; Doria, A. Optimization of a Piezoelectric Wind-Excited Cantilever for Energy Harvesting from Facades. In *Advances in Italian Mechanism Science*; Niola, V., Gasparetto, A., Quaglia, G., Carbone, G., Eds.; Springer Nature: Cham, Switzerland, 2022; pp. 848–856. [\[CrossRef\]](#)
27. Dicken, J.; Mitcheson, P.D.; Stoianov, I.; Yeatman, E.M. Power-extraction circuits for piezoelectric energy harvesters in miniature and low-power applications. *IEEE Trans. Power Electron.* **2012**, *27*, 4514–4529. [\[CrossRef\]](#)
28. Hobeck, J.D.; Inman, D.J. Artificial piezoelectric grass for energy harvesting from turbulence-induced vibration. *Smart Mater. Struct.* **2012**, *21*, 105024. [\[CrossRef\]](#)
29. *Standard EN 1991-1-4 (2005)*; Eurocode 1: Actions on Structures-Part 1–4: General Actions-Wind Actions. European Committee for Standardization: Brussels, Belgium, 2010.
30. Tao, T.; Wang, H.; Wu, T. Comparative Study of the Wind Characteristics of a Strong Wind Event Based on Stationary and Nonstationary Models. *J. Struct. Eng.* **2017**, *143*, 04016230. [\[CrossRef\]](#)
31. Roncallo, L.; Gimondo, M.; Tubino, F. Dynamic Response of Slender Vertical Structures Subjected to Thunderstorm Outflows. *Appl. Sci.* **2023**, *13*, 11440. [\[CrossRef\]](#)
32. Hao, H.; Ang, T.C. Analytical Modeling of Traffic-Induced Ground Vibrations. *J. Eng. Mech.* **1998**, *124*, 921–928. [\[CrossRef\]](#)
33. Au-Yang, M.K. Joint and Cross Acceptances for Cross-Flow-Induced Vibration—Part I: Theoretical and Finite Element Formulations. *J. Press. Vessel Technol.* **2000**, *122*, 349–354. [\[CrossRef\]](#)
34. Tommasino, D.; Moro, F.; Bernay, B.; De Lumley Woodyear, T.; de Pablo Corona, E.; Doria, A. Vibration Energy Harvesting by Means of Piezoelectric Patches: Application to Aircrafts. *Sensors* **2022**, *22*, 363. [\[CrossRef\]](#)
35. Kuang, Y.; Zhu, M. Evaluation and validation of equivalent properties of macro fibre composites for piezoelectric transducer modelling. *Compos. Part B Eng.* **2019**, *158*, 189–197. [\[CrossRef\]](#)
36. Tommasino, D.; Tonan, M.; Moro, F.; Doria, A. Identification of the Piezoelectric Properties of Materials From Impulsive Tests on Cantilever Harvesters. In *Proceedings of the International Design Engineering Technical Conferences and Computers and Information in Engineering Conference*, Boston, MA, USA, 20–23 August 2023; Volume 12, p. V012T12A005. [\[CrossRef\]](#)
37. Tummers, M.J.; Jacobse, J.; Voorbrood, S.G. Turbulent flow in the near field of a round impinging jet. *Int. J. Heat Mass Transf.* **2011**, *54*, 4939–4948. [\[CrossRef\]](#)

38. Hassan, M.E.; Assoum, H.; Sobolik, V.; Vétel, J.; Abed-Meraïm, K.; Garon, A.; Sakout, A. Experimental investigation of the wall shear stress and the vortex dynamics in a circular impinging jet. *Exp. Fluids* **2012**, *52*, 1475–1489. [[CrossRef](#)]
39. Yao, S.; Guo, Y.; Jiang, N.; Liu, J. An experimental study of a turbulent jet impinging on a flat surface. *Int. J. Heat Mass Transf.* **2015**, *83*, 820–832. [[CrossRef](#)]

**Disclaimer/Publisher’s Note:** The statements, opinions and data contained in all publications are solely those of the individual author(s) and contributor(s) and not of MDPI and/or the editor(s). MDPI and/or the editor(s) disclaim responsibility for any injury to people or property resulting from any ideas, methods, instructions or products referred to in the content.